RSC Advances

PAPER

View Article Online
View Journal | View Issue

Cite this: *RSC Adv.*, 2025, **15**, 19305

Green synthesis of ultrathin WS_2 nanosheets for efficient hydrogen evolution reaction†

Nadeesha L. Kothalawala, [a] Nipun Chandrasiri, [a] Manisha De Alwis Goonatilleke, [a] Keerthan R. Rao,[ab] Sujan Shrestha, [c] Udari S. Kodithuwakku,[a] Irene Y. Kim,[d] Chad Risko, [ab] Ambrose Seo, [c] Beth S. Guiton, [a] Fuqian Yang[e] and Doo Young Kim *[a]

Transition metal dichalcogenide (TMD) nanostructures have emerged as promising electrocatalysts for the hydrogen evolution reaction (HER) as there is an increasing demand for cost-effective and sustainable hydrogen production. Despite significant progress, there is still a critical need for developing facile and green methods for synthesizing ultrathin TMD nanostructures. In this study, we introduce a green, top-down synthesis method to produce highly exfoliated WS_2 nanosheets. The process combines the ultrasonication of bulk WS_2 in a binary water–ethanol solvent with a solvothermal treatment. The resulting ultrathin WS_2 nanosheets exhibit clean surfaces free of surface ligands and impurities, high crystallinity in the semiconducting hexagonal phase, and outstanding electrochemical activity for HER. Key performance metrics include a low onset potential of −0.32 V (*vs.* reversible hydrogen electrode (RHE)) at 10 mA cm^{-2} and a low Tafel slope of 160 mV dec^{-1} with a catalyst loading of 0.76 mg cm^{-2}. The promising HER performance is attributed to (1) a high density of exposed edges and defects, (2) enhanced charge transport due to high crystallinity, and (3) clean surfaces enabling efficient interfacial electron transfer. Furthermore, *operando* Raman spectroscopy using a 3D-printed electrochemical cell identifies the catalytically active sites on WS_2 nanosheets for HER. This work provides a green route to high-performance, low-dimensional electrocatalysts for sustainable hydrogen production.

Received 30th January 2025
Accepted 2nd June 2025

DOI: 10.1039/d5ra00712g

rsc.li/rsc-advances

Introduction

Layered transition metal dichalcogenides (TMDs) are emerging materials for a wide range of applications, including semiconductors,[1] sensors,[2] energy storage[3] and catalysis.[4,5] The electronic properties of bulk TMDs span from semiconductors (WS_2, MoS_2), to semimetals ($TiSe_2$, WTe_2), and to metals (NbS_2), making them highly versatile.[6] Their abundance, affordability, and layered structure make TMDs particularly suitable for electrocatalysis. The electrochemical activity of TMDs can be enhanced through strategies such as exfoliation, doping (substitutional and adatom), and the construction of heterostructures.[6,7] Exfoliation generates ultrathin nanosheets with high surface areas and abundant exposed edges, which serve as active sites for catalytic reactions. Doping and heterostructures[6,8] further modulate the electrochemical properties of TMDs, enabling efficient and selective catalysis. Heterostructures can be created by stacking TMD layers or decorating TMD surfaces with nano-catalysts, such as single atoms, clusters, or nanoparticles. These configurations allow precise tuning of electronic interactions between TMD layers or between TMD supports and catalysts, optimizing their catalytic performance.[8–10]

The transition to clean energy and achieving net-zero carbon emissions are critical goals for modern society. Hydrogen, as a clean and versatile energy carrier, offers significant potential for energy storage, transport, distribution, and utilization. Among various production methods, electrocatalytic water splitting powered by renewable energy sources stands out as a sustainable and eco-friendly approach to hydrogen generation. While Pt-based catalysts are the most efficient for hydrogen evolution reaction (HER), their high cost and scarcity hinder a widespread use in economical hydrogen production. To address this limitation, ultrathin TMD nanosheets, such as MoS_2 (ref. 11–13) and WS_2,[14,15] have emerged as promising alternatives, demonstrating notable HER activities when

[a]*Department of Chemistry, University of Kentucky, Lexington, Kentucky 40506-0055, USA*

[b]*Center for Applied Energy Research, University of Kentucky, Lexington, Kentucky 40506, USA*

[c]*Department of Physics and Astronomy, University of Kentucky, Lexington, Kentucky 40506-0055, USA*

[d]*Department of Psychology, University of California, Los Angeles, California 90095, USA*

[e]*Department of Chemical and Materials Engineering, University of Kentucky, Lexington, Kentucky 40506, USA*

† Electronic supplementary information (ESI) available. See DOI: https://doi.org/10.1039/d5ra00712g

prepared *via* liquid phase exfoliation (LPE). In the LPE of WS_2, an intercalation process transforms the semiconducting hexagonal phase into the metallic trigonal phase, enhancing electrocatalytic activity.[14] Wang *et al.* reported that the HER activity of WS_2 nanosheets originates from exposed edge sites, which promote efficient charge transfer.[15]

Despite extensive research, green, impurity-free, and scalable synthesis methods for TMD nanostructures have yet to be realized. Current synthetic approaches suffer from lengthy reaction times, high reaction temperatures, and labor-intensive purification steps. LPE offers the advantage of a simple and potentially scalable synthesis; however it typically relies on high-boiling-point organic solvents,[16] surfactants or polymers,[13,17] and reactive chemicals such as lithium intercalants.[11] These practices often result in residual impurities in the final products, which can interfere with electrochemical processes[18] and block catalytically active sites, limiting their performance.

Recent efforts have focused on developing cleaner LPE processes for TMD nanostructures that eliminate the use of intercalants or surfactants.[18] In these processes, the solvent's surface energy must match that of the TMD to enable efficient breakdown and exfoliation.[17,19–22] Trapped solvent molecules between the TMD layers induce a steric repulsion, weakening van der Waals interactions and facilitating exfoliation.[23] However, the use of high-boiling-point organic solvents in LPE, such as *N*-methyl-2-pyrrolidone (NMP) and dimethylformamide (DMF), is not ideal due to their environmental toxicity, the difficulty of removing solvent residues, and the risk of impurity formation in the final product.[24] Conversely, low-boiling-point solvents, which are also more environmentally friendly, have shown promise in achieving highly exfoliated layered nanostructures while minimizing these issues.[22,25]

In this work, we present a versatile and greener exfoliation method for WS_2, a less explored material than MoS_2 for HER. This approach is based on a modified LPE through ultrasonication and a solvothermal process in a water–ethanol solvent mixture. The method yields ultrathin, crystalline WS_2 nanosheets with diameters of a few hundred nanometers while avoiding the need for long sonication times, high temperatures, surfactants, or intercalants. Characterization techniques, including Raman spectroscopy, atomic force microscopy (AFM), X-ray diffraction (XRD), and high-resolution transmission electron microscopy (HR-TEM), confirm the successful exfoliation of WS_2 into mono- to few-layered nanosheets with high crystallinity and clean surfaces. Scanning transmission electron microscopy (STEM) reveals structural defects that may act as catalytically active sites, while X-ray photoelectron spectroscopy (XPS) and HR-TEM confirm that the predominance of the semiconducting prismatic (2H) phase. The resulting WS_2 nanosheets demonstrate excellent electrochemical HER performance, comparable to or exceeding previous studies. *Operando* Raman spectro-electrochemical measurements affirm that sulfur surface sites are the catalytically active centers for HER, as indicated by Raman bands in the low-wavenumber region corresponding to S–H bending (812 cm^{-1}) and wagging (722 cm^{-1}) modes, further supported by periodic density functional theory (DFT) models.

Experimental section

Synthesis methods

All chemicals and solvents used in the synthesis of the WS_2 nanosheets were purchased commercially. Tungsten(IV) sulfide (powder, 2 μm, 99%) and ethyl alcohol (Pure, 200 proof, ACS reagent, ≥99.5%) were purchased from Sigma Aldrich. Deionized (DI) water was obtained from a Barnstead™ E-pure™ ultrapure water purification system.

Prior to exfoliation, the mixture of ethanol and DI water (30 : 70 v/v) was degassed to remove dissolved oxygen. WS_2 bulk powder (0.5 gram) was added to a Schlenk flask, and degassing was performed to remove oxygen. 100 mL of the degassed solvent was added to the Schlenk flask with WS_2 powder. The mixture was subjected to ultra-probe sonication (Sonics & Materials, Model VCX500) at 55% amplitude for 1.5 hours (2 seconds on and 2 seconds off). 60–70 mL of the ultra-sonicated mixture was heated at 85 °C for 6 hours under an inert environment. The mixture was then centrifuged at 4000 rpm (relative centrifugal force or g-force: 1010) for 7 minutes to separate the less-exfoliated WS_2 (intermediate product) from ultrathin WS_2 nanosheets (final product). The supernatant was subjected further to ultra-centrifugation at 12 000 rpm (relative centrifugal force or *g*-force: 1304) to separate the highly exfoliated ultrathin WS_2 nanosheets. The final product was washed three times with the fresh portion of the same solvent mixture to remove any impurities. The obtained ultrathin WS_2 nano-sheets were dried in a vacuum oven at 60 °C for further analysis. The typical yields of highly exfoliated ultrathin WS_2 nanosheets (final product) and less-exfoliated WS_2 nanosheets (intermediate product) were 3% and 76%, respectively. The low yield of highly exfoliated (mono- and few-layered) WS_2 nanosheets can be addressed by upgrading the exfoliation apparatus and equipment – for example, optimizing the probe size and vibration amplitude in the probe sonicator, as well as adjusting the solvent volume in the solvothermal step.

Spectroscopic and microscopic characterizations

Raman measurements were carried out by a DXR Raman microscope (Thermo Scientific) with a diode pump Nd:YVO_4 laser. Raman spectra of WS_2 nano-sheets were acquired with a 532 nm laser at 1 mW laser power by mounting WS_2 nanosheets (powder form) on a well cleaned Si wafer. The measurements were performed with a 2 second exposure time, 20 exposures, and with a 2.1 μm spot size. XPS analysis was completed using a K-alpha X-ray photoelectron spectrometer (Thermo Scientific) equipped with a monochromatic Al Kα X-ray source of 1486.6 eV energy. The spot size was 400 μm. Powder X-ray diffraction (XRD) measurements were carried out using a Bruker AXS X-ray spectrometer with a Cu tube (1.54 Å). The detector used was an energy dispersive LYNXEYE (1D mode) detector. All XRD measurements were carried out with 0.8 s per step and an increment of 0.01 s. The powder samples were scanned in the 2θ range of 10° to 80°. The surface topography of the WS_2 nanosheets was characterized by AFM (Park system XE-70) in tapping mode. The samples were prepared by spin casting

diluted dispersion (200 μL) of WS_2 nanosheets in isopropyl alcohol on a clean mica plate at a rotation speed of 2000 rpm. The mica plate with the sample was dried overnight in the oven at 60 °C.

UV-Vis absorbance measurements were performed on a Thermo-Scientific Evolution 201 UV-Visible spectrophotometer. A dispersion of nanosheets in a 30% ethanol–water solvent mixture was used to measure the absorbance in the wavelength range of 200–1000 nm with 0.1 s integration time and 1 nm bandwidth.

Scanning electron microscopy (SEM) imaging was carried out with a field emission Hitachi S4300 microscope with an accelerating voltage of 10 kV for the ultrathin WS_2 nanosheets. Transmission electron microscopy (TEM) images and energy dispersive X-ray spectroscopy (EDS) data were collected on an FEI Talos F200X TEM/STEM electron microscope at 200 kV equipped with a Super-X EDS detector. Drop casting was used to prepare the TEM samples. Briefly, small amount of ultrathin nanosheets were suspended in analytical-grade isopropyl alcohol and sonicated for about 20 minutes. About 10 μL of the suspension was drop-cast onto a 300 mesh Cu TEM grid coated with holey carbon.

A Nion Ultra STEM 100 (U100) aberration-corrected electron microscope operated at 100 kV was used to obtain atomic resolution high-angle annular dark field (HAADF) scanning TEM (STEM) images. The Ultra STEM is a 5th-order aberration-corrected microscope with a 0.1 nm maximum spatial resolution at 100 kV. The samples were prepared similarly to the TEM samples with further annealing at 160 °C for 10 hours in a high vacuum oven prior to STEM imaging.

High-resolution TEM/STEM images were processed using the fast Fourier transform (FFT). The diffraction spots generated in reciprocal space on the FFT patterns were selectively masked and transformed to real space, creating inverse FFT (IFFT) images from the masked frequencies. Image processing was conducted on Gatan Digital Micrograph® software. Crystal structural models of the prepared WS_2 were generated using CIF files on CrystalMaker® software.

Electrochemical characterization

Three mixtures for electrochemical characterization were prepared, starting with mixing ultrathin WS_2 nanosheets and carbon black (10 wt%, 50 wt%, and 80 wt% of WS_2 nanosheets). 20 μL of Nafion ionomer (fuel cell store, Nafion dispersion D520) and 1 mL of deionized water were added to each mixture, then sonicated in a bath sonicator for 45 minutes until an ink consistency was obtained. 20 μL of the catalyst ink was drop-cast on a rotating disk electrode (RDE). The casting of the catalyst ink was repeated twice more to deposit 60 μL on RDE. The RDE with the deposited catalyst was then placed in an oven at 60 °C overnight.

Electrochemical measurements were carried out with a CHI potentiostat (CH Instruments, model: 660D). Electrochemical HER tests were conducted using a RDE with the catalyst mounted as the working electrode, reversible hydrogen electrode (RHE) as the reference electrode, and a graphite rod as the counter electrode. Details of the RHE setup are provided in the ESI.† The electrolysis was carried out in 0.5 M H_2SO_4 at a rotating speed of 1600 rpm. Ultra-pure N_2 was purged through the electrolyte for 45 minutes before electrolysis. The preconditioning of the catalyst was performed under cyclic voltammetry (CV) with 50 cycles at 0.02 V s^{-1} scan speed in a potential range from 0.1 to −1.0 V (v. RHE) at a rotating speed of 1600 rpm. Linear sweep voltammetry (LSV) was then performed with a scan rate of 20 mV s^{-1} in the same potential range. All LSV curves were *iR* corrected using the solution resistance (R_Ω) measured by electrochemical impedance spectroscopy (EIS). HER stability measurements were performed by cycling the potential in the same range for 4 hours at a scan speed of 0.02 V s^{-1} at a rotating speed of 1600 rpm. Amperometry was also performed to determine the catalyst stability by applying a constant potential (−0.4 V *vs.* RHE) for 3 hours at a rotating speed of 1600 rpm.

Operando Raman spectro-electrochemistry

An *operando* Raman cell was designed using an Autodesk Fusion 360 software package. The cell was designed to accommodate several components: (1) a screen-printed-electrode (SPE, Pine research) holder, (2) an electrolyte chamber where the SPE is immersed in electrolyte, (3) a microfluidic channel for the flow of electrolyte, and (4) an optical window for Raman spectroscopy. For the optical window, UV fused silica high-precious window was purchased from Thorlabs (WG41010 – Ø1″ UVFS broadband precision optical window, uncoated, thickness = 1 mm). The optical window was placed between two O-rings and further secured with silicone to prevent any leakage. The *operando* Raman cell was printed using a 3D printer (Anycubic Photon D2) and with a UV (405 nm) sensitive resin. Before Raman measurement, 0.5 M H_2SO_4 was circulated through the printed cell for 2 hours to warrant no leftover of uncured or broken resin residues in the cell.

The SPE was precleaned before depositing catalyst as follows. CV was carried out in a potential range from 2.5 V to −2.5 V with three segments at a scan rate of 0.1 V s^{-1} in 0.5 M H_2SO_4. This is an essential step to remove carbon cross-linking and to increase surface roughness of SPE. The electrode was then dried, and 6 μL of the 50 wt% WS_2 catalyst ink (1 mg WS_2 nanosheets + 1 mg carbon black + 20 μL Nafion + 1 mL DI water) was drop-casted onto the electrode. Drop casting was repeated three times to deposit 18 μL of the catalyst ink. Finally, the electrode was dried and inserted into the 3D printed *operando* Raman cell.

Prior to an *operando* Raman measurement, an external reservoir was filled with 0.5 M H_2SO_4, then purged with N_2 for 45 minutes. Inlet and outlet tubes to the reservoir were then connected to the corresponding ones of the cell. The electrolyte was circulated through the cell with a peristaltic pump. Finally, chronoamperometric measurements were carried out at a potential of −0.4 V, −0.6 V, −0.8 V, −1.0 V and −1.2 V for 60 seconds while a Raman spectrum was recorded at each potential. Raman spectra were acquired with 532 nm laser excitation

(0.8 mW power, 2 second exposure time, 30 exposures, 50 μm slit) and 10× objective.

DFT calculations

DFT calculations were carried out using the Vienna *Ab Initio* Simulation Package (VASP).[26–28] Plane wave basis sets were used to solve the Kohn–Sham equations. To describe the electron–ion interactions, the projector-augmented wave (PAW) method,[29] which is a frozen core all-electron method with the exact shape of the valence wave functions, was used. The Perdew–Burke–Ernzerhof (PBE) functional within the generalized gradient approximation (GGA) was used to calculate exchange–correlation energies.[30] For ionic relaxation, the conjugate gradient algorithm was employed.[31] Periodic boundary conditions with a plane-wave-energy cutoff of 400 eV were used for geometric optimization. A hexagonal crystal structure was obtained from the Materials Project database (mp-224).[32] The relaxed 3 × 3 bulk structure was repeated in the *x*- and *y*-direction to obtain a periodic slab with a vacuum of 15 Å to prevent interaction between repeated slab layers. The bottom S–W–S layer was fixed to represent the bulk structure, and the top S–W–S layer was allowed to relax with 9 S atoms on the surface (Fig. S6a†). Self-consistent field (SCF) calculations for adsorption were converged to 1×10^{-6} eV $Å^{-1}$. A Methfessel–Paxton (MP) smearing of 0.2 eV and a Monkhorst–Pack grid of 3 × 3 × 1 was used for the Brillouin zone integration for the isolated slab and calculation of the adsorption energy. To determine the vibrational frequencies, dynamical matrix calculations were carried out according to the methods described by Henkelman *et al.* with a displacement of 0.001 Å for the adsorbed H-atom and 8 S atoms on the surface (total of 9 atoms displaced resulting in 27 degrees of freedom).[33]

Results and discussion

The synthetic procedure of the WS_2 nanosheets, consisting of three steps, is outlined in Scheme 1. A 30 : 70 (v/v) ethanol–water mixture was chosen to make the surface energy of the solvent mixture (33 m Nm^{-1} at 25 °C)[34] close to that of WS_2 (30 m Nm^{-1})[22] for efficient exfoliation. By choosing a solvent with surface energy similar to the surface energy of the layered material, exfoliation can be facilitated by overcoming the van der Waals interactions between layers.[18,19] Further, the interaction among the nanosheets and solvent can stabilize the dispersion of exfoliated nanosheets.[18,19] Moreover, the solvent molecules exert a steric repulsive force between layers to expedite the exfoliation process.[21,22,35] Bulk WS_2 dispersed in the ethanol–water mixture is subjected to ultrasonic waves which produce cavitation bubbles. During ultrasonication, the collapse of cavitation bubbles generates high energy jets that produce nanostructured WS_2 with reduced later dimensions and thickness. During the subsequent solvothermal process, the WS_2 layers are further separated into highly exfoliated nanosheets. It is worth noting that extreme care is taken in this synthesis to avoid the oxidation of WS_2 nano sheets by using a degassed solvent, purging N_2 during the ultra-sonication, and conducting the solvothermal step in a Schlenk line. The ultrathin WS_2 nanosheets (final product) were used for further characterization and electrochemical measurements.

Fig. 1a shows the Raman spectra of ultrathin WS_2 nanosheets at several spots and bulk WS_2 powder. For a better comparison, normalized spectra are displayed in the fingerprint region (Fig. 1b). There are two dominant peaks, E^1_{2g} and A_{1g}. The E^1_{2g} mode at 351 cm^{-1} corresponds to the in-plane vibrations of S–W–S. The A_{1g} peak at 418 cm^{-1} corresponds to the out-of-plane vibration of S–W–S. These two peaks and their positions are in a good agreement with the previous reports.[36]

Compared to bulk WS_2, ultrathin nanosheets of WS_2 show a slight red-shift in A_{1g} peak. This red shift is attributed to the weaker interlayer interaction in the exfoliated nanosheets. The intensity ratio of E^1_{2g} and A_{1g} serves as an important parameter to indicate the thickness of WS_2 nanosheets. The ratios of E^1_{2g} and A_{1g} intensities, $\frac{I_{E^1_{2g}}}{I_{A_{1g}}}$, measured at different spots on WS_2

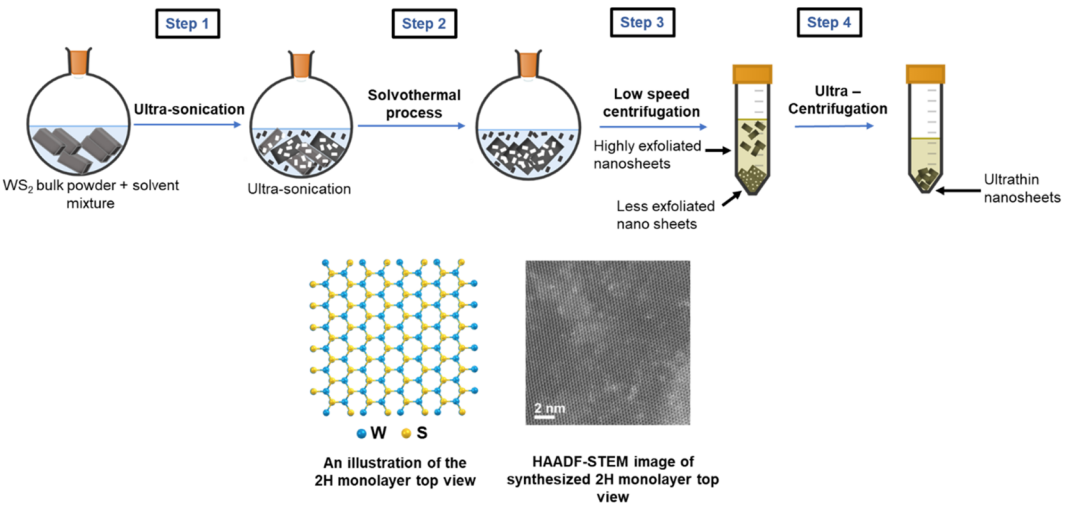

Scheme 1 The synthesis of ultrathin WS_2 nanosheets.

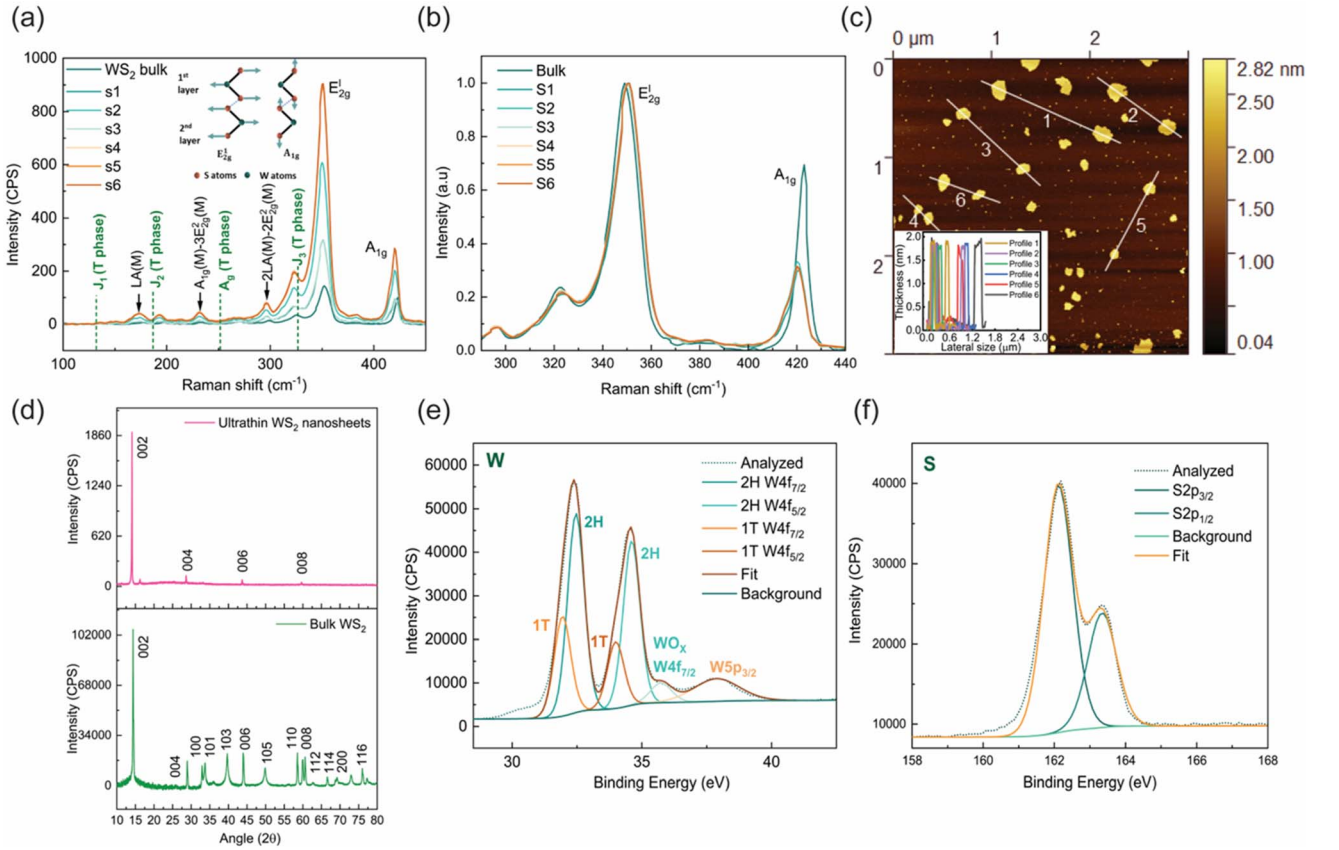

Fig. 1 (a) Raman spectra of exfoliated WS_2 nanosheets collected from six spots and WS_2 bulk powder. (b) Raman spectra of six spots normalized to the E^1_{2g} peak maximum. (c) AFM image of exfoliated WS_2 on a mica substrate. Scanned area of the image is 3 μm × 3 μm. Inset: line–scan profiles across several WS_2 nanosheets on the AFM image. (d) XRD spectra of the ultrathin WS_2 nanosheets (top) and bulk WS_2 (bottom). (e) XPS high resolution spectra of W4f and (f) XPS high resolution spectra of S2p.

nanosheets are listed in Table S1.† The ratios of exfoliated WS_2 nanosheets (3.0–3.3) are significantly higher than that of the bulk (1.90), because of the weakening of van der Waals forces between layers. The ratio of >2 suggests that the exfoliated nanosheets are predominantly mono-layered.[36–38] E^1_{2g} and A_{1g} peaks in the Raman spectra are characteristic of mono-layered hexagonal (1H) phase, confirming that semiconducting phase of bulk WS_2 powder is retained after exfoliation.[39] The characteristic peaks of metallic 1T-WS_2 nanosheets in the low frequency regions are 131 cm^{-1}, 188 cm^{-1}, 258 cm^{-1} and 325 cm^{-1} (J_1, J_2, A_g, and J_3 modes respectively).[14,39] These peaks are not observed at any spots of our exfoliated sample due to the low concentration of 1T phase formed during our synthesis.[37]

Fig. 1c shows the AFM image of the WS_2 nanosheets. The line–scan profiles across several nanosheets are shown in the inset. The line–scan profiles indicate that the nanosheets have an average thickness of 1.6 nm. It is known that the thickness of a WS_2 monolayer is ∼1 nm.[14] Hence, the ultrathin WS_2 nanosheets on atomically flat mica are either mono-layered or bi-layered. The thicknesses and the diameters of WS_2 nanosheets determined by AFM are summarized in Table S2.†

Powder XRD patterns of WS_2 nanosheets and bulk WS_2 are shown in Fig. 1d. While bulk WS_2 displays all characteristic peaks of 2H phase, WS_2 nanosheets exhibit sharp but simpler peaks. The sharp peaks indicate that WS_2 nanosheets retain the crystallinity of hexagonal phase after exfoliation.[22,40] It is noteworthy that all non-vertical planes are absent in the XRD pattern of ultrathin WS_2 nanosheets.[40–42] This implies that the exfoliation is successful and exfoliated WS_2 nanosheets are primarily mono-layered.

Fig. 1e and f show the high-resolution XPS spectra for W4f and S2p, respectively. The deconvolution of W4f XPS peak reveals that the majority of WS_2 nanosheets are 1H phase also with the minor 1T phase converted from 1H phase. Two W4f XPS peaks at 31.9 eV and 34.0 eV in the low binding energy region correspond to the 1T-phase $W4f_{7/2}$ and $W4f_{5/2}$ respectively, whereas the peaks at 32.46 eV and 34.61 eV correspond to the 1H-phase $W4f_{7/2}$ and $W4f_{5/2}$, respectively. These binding energies are in a good agreement with previous XPS studies of 1H WS_2 and 1T WS_2 nanostructures.[14,37] The peak at 35.74 eV can be assigned to the oxidized $W(W^{6+})$ $4f_{7/2}$ and originates from the minor oxidation of W sites during the synthesis. The high-resolution XPS spectrum of S shows two peaks at 162.1 eV and 163.4 eV for $S2p_{3/2}$ and $S2p_{1/2}$, respectively, in agreement with previous studies.[14,37] The XPS survey spectra of the WS_2 nanosheets shown in Fig. S1b† suggests that the samples are free of impurities. In the survey spectra, carbon and oxygen peaks are due to exposure to the atmosphere and from carbon

tape used for XPS measurement. Elemental compositions and the binding energies of elements are summarized in Table S3.† The atomic ratio of W and S is close to 1 : 2.

The UV-Vis absorbance spectrum of WS_2 nanosheets is presented in Fig. S1a.† There are three well-resolved absorption bands at 640 nm (A peak), 530 nm (B peak), and 475 nm (C peak), due to the excitonic transitions.[40,43] Hence, the intense and well-resolved absorption bands confirm a direct band gap in WS_2 nanosheets due to the reduced number of layers. Further, the direct band-gap transition at 640 nm (1.94 eV) shows the formation of mono-layered WS_2, consistent with previous reports.[25,44]

The morphology, shape, and dimension of WS_2 nanosheets were determined by SEM as shown in Fig. 2a. The exfoliated WS_2 nanosheets present both hexagonal and irregular shapes. The distribution of particle sizes of a total of 200 particles (Fig. 2b) yields an average size of 195 ± 55 nm, which is further confirmed by low-resolution TEM image in Fig. 2c. The hexagonal atomic arrangement of W atoms and the microstructure of the prominent 1H phase of WS_2 in Fig. 2e show an interlayer spacing of 0.27 nm corresponding to (100) layers of WS_2. The selected area electron diffraction (SAED) pattern in Fig. 2f confirms the single-crystalline nature of the nanosheets with the sheet perpendicular to the [001] direction of WS_2. Energy-

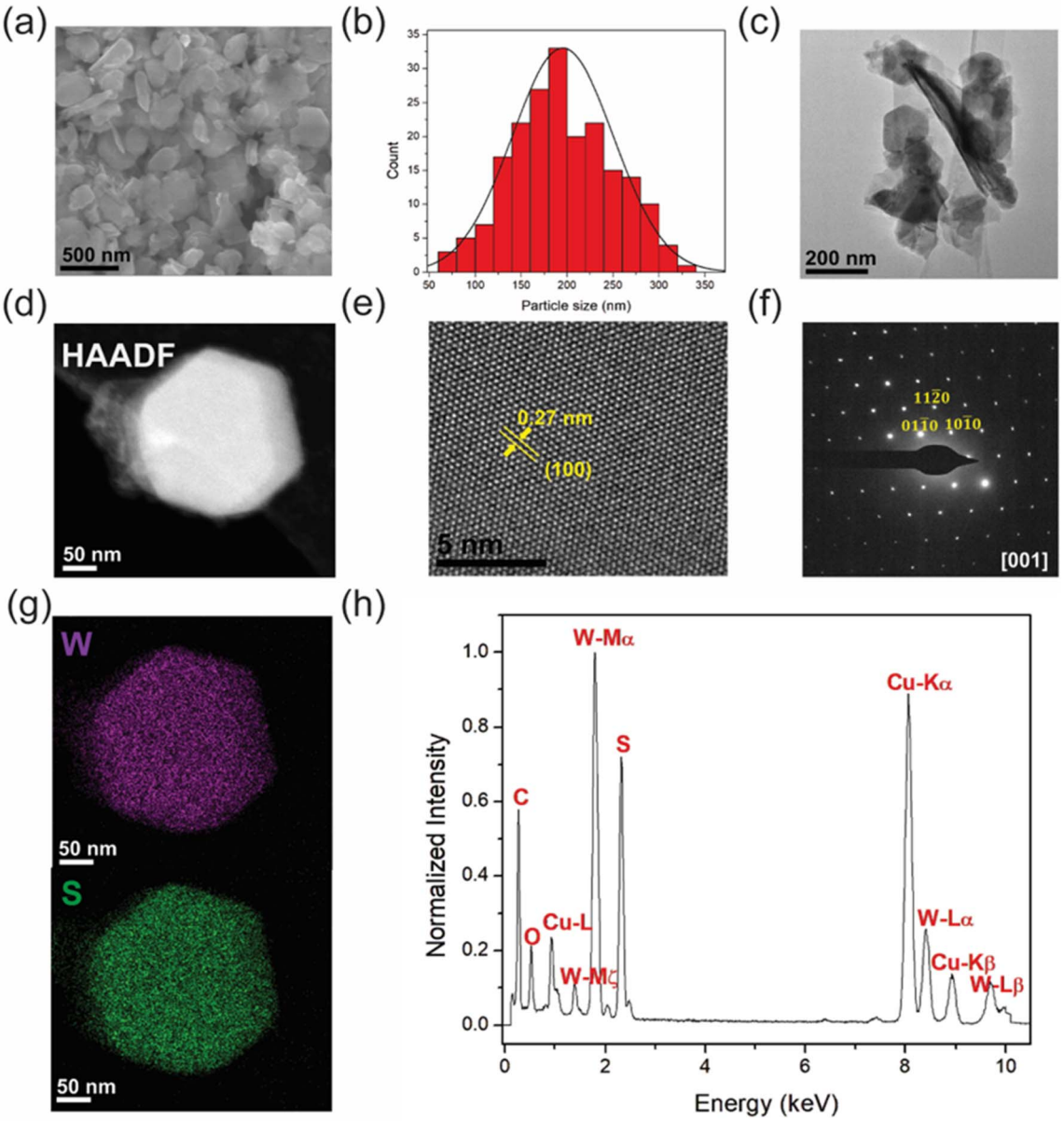

Fig. 2 (a) SEM image of the ultrathin WS_2 nanosheets. (b) Distribution of particle sizes of ultrathin nanosheets. (c) Low-resolution TEM image of ultrathin WS_2 nanosheets. (d) HAADF-STEM image of an ultrathin WS_2 nanosheet. (e) HR-TEM image of a WS_2 nanosheet showing lattice fringes of 0.27 nm corresponding to (100) plane of WS_2. (f) SAED pattern of WS_2 nanosheets indexed to the (001) zone axis of the 1H phase. (g) EDS elemental maps of W and S. (h) EDS spectrum indicating the elemental composition of WS_2 (Cu peak originates from the TEM sample grid).

dispersive X-ray spectroscopic (EDS) analysis was performed to confirm the elemental composition of WS_2 nanosheets. The EDS elemental maps and spectra are given in Fig. 2g and h, respectively. The homogeneous distribution of W (purple) and S (green) throughout the nanosheet is clearly shown, and the spectrum gives intense peaks at ~1.77 keV and ~2.30 keV, corresponding to W-Mα and S-Kα peaks, and other minor peaks of tungsten. The sharp peaks at ~0.27 keV (C-Kα) and ~8.04 keV (Cu-Kα) originate from the Cu sample grid with C overlay, used in the TEM analysis. The presence of a small amount of O at ~0.52 keV was also detected.

Fig. 3 shows the atomic resolution HAADF-STEM micrographs of ultrathin WS_2 nanosheets. A mono-layered nanosheet is shown in Fig. 3a, where the atomic arrangement is clearly visible. An enlarged inverse Fast-Fourier-transform (IFFT) image of the nanosheet is given in Fig. 3b which overlaps with the simulated structural model of WS_2 in the 1H phase along [001] axis. The W and S atoms are indicated in purple and green colors, respectively. Fig. 3c is the intensity profile along the yellow arrow in Fig. 3b, distinguishing the difference between the intensities of W and S. The intensity profile indicates that W ($Z = 74$) is more intensely than S ($Z = 16$), confirming their positions in the structure.[45,46] The inter-atomic distance of W atoms is 0.54 nm which matches well the simulated distance of 0.546 nm between W atoms on the (001) plane of WS_2. It is noteworthy that the ultrathin WS_2 nanosheets produced from

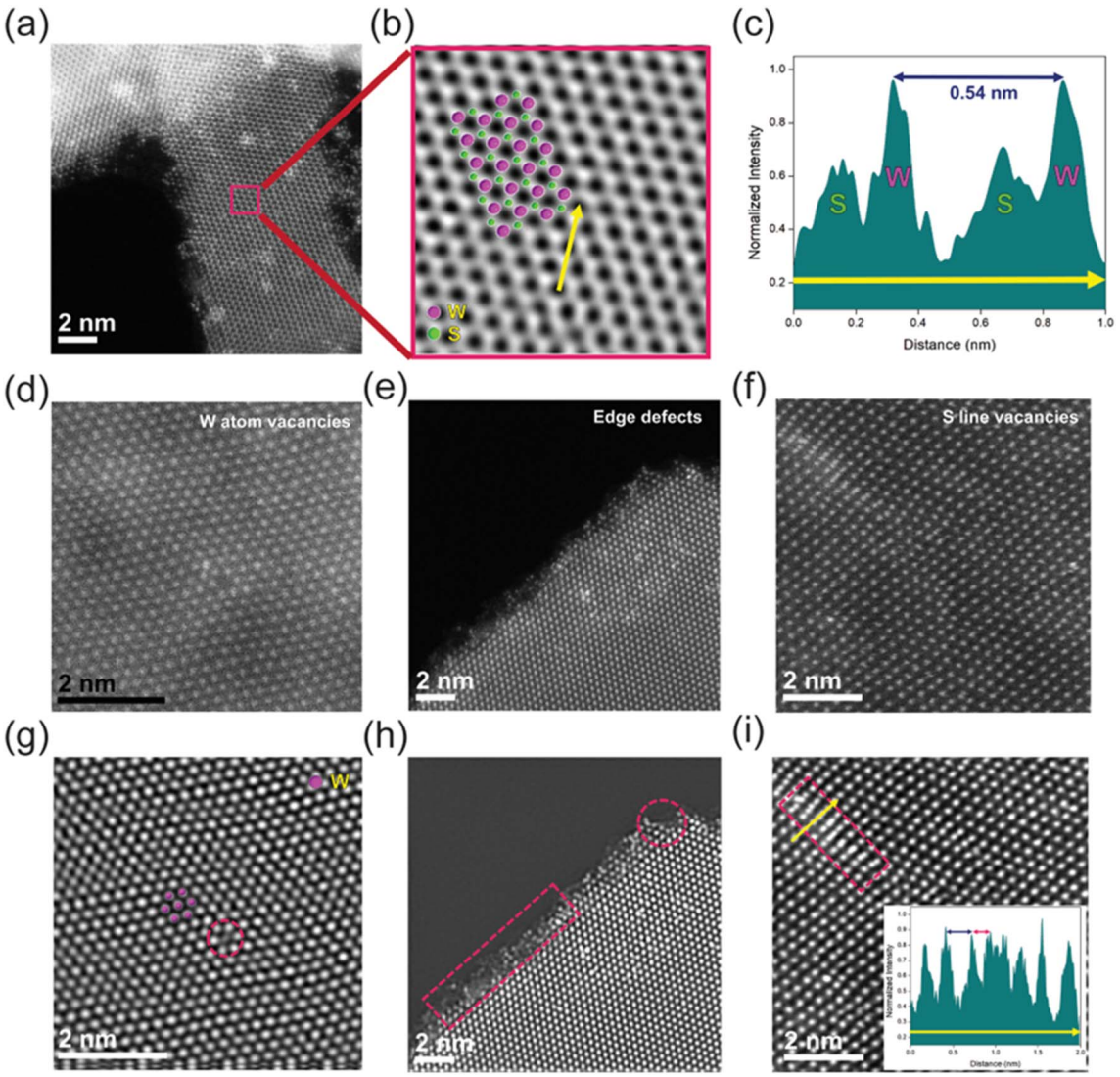

Fig. 3 (a) HAADF-STEM image of monolayer WS_2 nanosheets. (b) Enlarged inverse FFT (IFFT) image of the area shown in the pink square of image (a), showing hexagonal-atomic arrangement of the 1H phase of WS_2, overlayed with the WS_2 1H crystal structure model obtained from the CrystalMaker software. W atoms are given in purple color and S in green color. (c) Intensity profile across the yellow arrow in image (b) indicating the W and S intensities. Inter-atomic distance of 0.54 nm between W atoms in the 1H phase is shown. (d–f) Atomic resolution HAADF-STEM images showing different types of structural defects in the nanosheets. (g–i) IFFT images of the HAADF-STEM images in (d)–(f) respectively, highlighting the defect areas. The intensity profile along the yellow arrow is given on the inset indicating the reduction in interlayer distance of W atomic layers due to S vacancy lines created.

this method result in a small percentage of the 1T phase of WS_2 (Fig. S2a–c†) which is also revealed in the XPS data. In monolayer WS_2, two S layers sandwich a W layer resulting in a slab with a thickness of 3.14 Å. The 1H phase exhibits a trigonal prismatic geometry around W with the stacking sequence of AbA (the upper-case and lower-case letters denote S and W, respectively), therefore placing the second S layer directly above the first. In contrast, the 1T phase shows an octahedral geometry with an AbC stacking sequence, with the W occupying the octahedral holes of S.[6] Due to the intensity variation caused by the different stacking sequences of the two phases, *Z* contrast imaging can distinguish the areas containing the two phases.[47] The comparison of atomic arrangement between 1H and 1T phases along with their respective structural models are given in ESI (Fig. S2d†).

STEM characterization has been further used to identify structural defects in ultrathin nanosheets that can be catalytically active for the HER. Three different types of defects visible on the WS_2 nanosheets are given in Fig. 3d–f. A loss of a W atom resulting in a point defect is clearly seen in the HAADF-STEM image of a WS_2 monolayer in Fig. 3d, and the defect site is highlighted in its IFFT in Fig. 3g. Most defect sites are present at the edges of the nanosheets as the atoms at surface edges contain dangling bonds and can be easily knocked off due to low displacement energy. Such defects can be seen in Fig. 3e (and its corresponding IFFT in Fig. 3h). Another type of defects observed are S vacancy lines, as shown in Fig. 3f. Since the displacement energy of S is low compared to W, they can be easily lost from the structure and eventually form vacancy lines. The loss of S rows from the structure results in the remaining W atomic columns contracting together as highlighted in the IFFT in Fig. 3i. This is confirmed with the intensity profile (inset of Fig. 3i) along the specified yellow arrow, with the size differences of the purple and pink double arrows indicating the interlayer distances. Increased number of S vacancy defects may eventually lead to a transition from semiconducting to conducting.[48] It should be noted that these defects may have been created due to knock-on damage by the high energy of the electron beam.[49] A previous study by Wu *et al.* demonstrated that the Tafel slope decreased as S-vacancy site density increased, suggesting their contributions to HER kinetics.[50]

Several previous studies reported electrochemical performances of doped and nanostructured WS_2 nanosheets for HER.[14,16,39,41,42,51–53] Here, the ultrathin WS_2 nanosheets obtained through LPE exhibit excellent HER activities. Fig. 4a presents *iR*-corrected LSV curves of WS_2 nanosheets in comparison with carbon black and commercial Pt/C (20 wt% Pt). To enhance electrical conductivity of ultrathin 1H-phase WS_2 nanosheets, catalyst samples were prepared by mixing WS_2 nanosheets with carbon black powder (WS_2 : carbon black 10 : 90, 50 : 50, 80 : 20 w/w). All WS_2 nanosheets showed better HER performances than carbon black. Among those, 80 wt% WS_2 exhibits the best HER activity with a low onset potential, −0.32 V *vs.* RHE (corresponding to 10 mA cm^{-2}, η_{10}) and highest current density. Its best performance is attributed to the largest amount of WS_2 with active sites available for HER.

Tafel plots (*iR*-corrected) are presented in Fig. 4b. The overpotential (η_{10}), and Tafel slope determined from the Tafel analysis, along with the catalyst loading (mg cm^{-2}), are summarized in Table S4.† In this study, three WS_2 catalyst mixtures present the similar Tafel slope of 163–168 mV $decade^{-1}$, indicating HER occurs through the same mechanism. Similar Tafel slopes were reported for exfoliated 2H-WS_2.[50,54] The Tafel slope of ∼160 mV $decade^{-1}$, characteristic of the Volmer mechanism indicate that the atomic hydrogen adsorption is the HER limiting step.[55] Based on the Tafel slope and the low defect concentration observed in the high resolution STEM images, H_2 generation in exfoliated WS_2 is more likely to involve one adsorbed proton and a second proton from unadsorbed water, rather than two adsorbed protons. Therefore, the overall mechanism is likely to follow Volmer–Heyrovsky pathway. Tafel slopes of Pt/C and carbon black are 65 mV dec^{-1} and 457 mV dec^{-1}, respectively. Table S5 in ESI† summarizes the overpotential (η_{10}) and Tafel slope of 2H-WS_2 in this study, in comparison with various WS_2 catalysts reported in recent literature. Our 2H-WS_2 catalyst exhibits a Tafel slope similar to those of other 2H-WS_2 catalysts, with a lower overpotential. WS_2 catalysts with phase conversion to 1T-phase, phosphorus incorporation, or strain engineering demonstrate significantly reduced Tafel slopes and overpotential.

Nyquist plots determined from EIS measurements are shown in Fig. 4c. The 80 wt% WS_2 shows the best charge transfer resistance (R_{ct}), suggesting that this catalyst contains largest concentration of active sites. The Nyquist plots were fitted with a simple circuit model and the fitting parameters, R_Ω, C_{dl}, and R_{ct}, for three catalyst mixtures are summarized in the ESI, Table S6.† We also compared the electrochemical surface area (ECSA) by measuring the double layer capacitance (C_{dl}) in Fig. 4d. Fig. S3† showed the cyclic voltammograms (CVs) of three WS_2 catalyst mixtures taken with various scan rates (10–140 mV s^{-1}). The 80 wt% WS_2 catalyst shows the largest ECSA, suggesting that this catalyst has larger active surface area and more active sites for hydrogen evolution.

We further examined the long-term stability of WS_2 nanosheets under HER. The long-term behavior was monitored in two ways: (1) continuous potential cycling for 4 hours, and (2) chronoamperometry at a fixed potential (−0.5 V *vs.* RHE) for 3 hours. Interestingly, different behaviors were observed. After continuous potential cycling, LSV showed a slight enhancement in the current (Fig. S4a†). Conversely, a gradual decay of HER current was observed at constant potential (Fig. S4b†).

To investigate the origin of activity decay in fixed-potential chronoamperometry, we analyzed WS_2 catalysts by *ex situ* XPS at three different stages: (i) before electrolysis (Fig. S4c and S4d†), (ii) after electrolysis (Fig. S4e and S4f†), and (iii) after immersing the electrode in the electrolyte for 5 hours without electrolysis (Fig. S4g and S4h†). The comparison of the WO_x $4f_{7/2}$ peaks in Fig. S4c and S4e† indicates the oxidation of WS_2 during electrolysis. A peak at 169.6 eV in the S2p XPS spectra of all three samples is predominantly from sulfonate group of the Nafion binder, but it could also partially originate from WS_2 oxidation.[39] *Ex situ* XPS analysis suggests that electrochemical oxidation of WS_2 is the primary cause of activity decay in

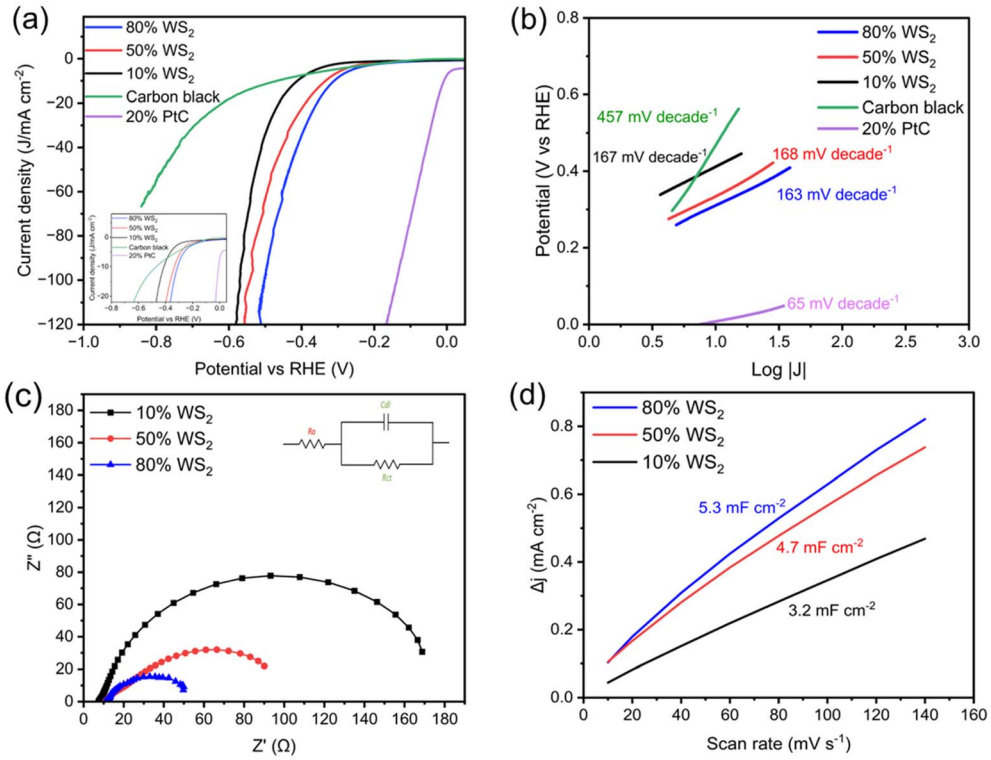

Fig. 4 (a) Polarization curves of three WS_2 catalyst mixture (10 wt%, 50 wt%, 80 wt%), only carbon black, and commercial 20 wt% Pt/C (inset shows a better representation of the onset potentials), (b) Tafel plots for WS_2, carbon black, and Pt/C with the calculated Tafel slopes for HER, (c) Nyquist plots of three catalyst mixture determined by EIS measurements (inset shows an equivalent circuit), and (d) electrochemical active surface areas estimated from the cyclic voltammograms at various scan rate (10–140 mV s^{-1}, Fig. S3†).

chronoamperometry, consistent with the literature.[39] Additionally, catalyst detachment and H_2 bubble formation may contribute to the current decay.

Notably the current slightly increases after extended potential cycling (from 0 V to −1.2 V) (Fig. S4a†), because surface oxides are removed by negative potential.[56] This preconditioning can activate the catalyst. Previous studies have reported that potential cycling can induce morphological changes in TMD nanosheets, leading to enhanced activity.[56]

To identify active sites and intermediate species for HER, we conducted *operando* Raman spectroscopy using a home-built, *operando* Raman cell and a screen-printed electrode (Fig. 5a–c). Fig. 5d shows *operando* Raman spectra of ultrathin WS_2 nanosheets collected at applied potentials. The peaks at 351 cm^{-1} and 418 cm^{-1} correspond to the E^1_{2g} and A_{1g} vibrational modes of WS_2, respectively. The additional peaks at 996 cm^{-1}, 1054 cm^{-1} are due to the asymmetric stretching of SO_4^{2-} electrolyte anions. The D, G and 2D bands appearing at 1351 cm^{-1}, 1590 cm^{-1} and 2700 cm^{-1}, respectively, are attributed to carbon black that is added to WS_2 catalyst.

Importantly, the *operando* Raman studies reveal three peaks in the low-frequency region at 214 cm^{-1}, 722 cm^{-1}, and 812 cm^{-1}, each of which evolve with applied potential. These three Raman bands are absent at open circuit potential. The zoomed-in Raman spectra in Fig. 5e show the progressive increase of the three Raman peaks with the applied potential. The voltage-dependent increase in Raman peaks is consistent with HER currents, as shown in Fig. S5a.†

There are a few reports on the similar low-frequency Raman bands assigned to H adsorption on the surface of TMDs. Afanasiev *et al.* and Wright *et al.* performed inelastic neutron scattering experiments and theoretical calculations for the gas-phase uptake of hydrogen on MoS_2 and WS_2,[57,58] identifying low-frequency Raman peaks (in the range from 650 cm^{-1} to 800 cm^{-1}) for S–H bending modes.[57,58] Based on these reports, the most probable assignment for 722 cm^{-1} and 812 cm^{-1} peaks are the wagging and bending vibrations of S–H bond connected to W. The peak at 214 cm^{-1} can be attributed to another S–H wagging mode. This assignment is supported by previous theoretical work on H_2S and H_2O adsorption on Ge surfaces,[59] which reported S–H wagging mode between 200 cm^{-1} and 300 cm^{-1}.

To confirm that the three Raman bands originate from the adsorption of protons on WS_2 nanosheets, we conducted a control experiment with carbon black alone. As shown in Fig. S5b,† carbon black alone did not exhibit these peaks. Fig. S5d† presents Raman spectra of WS_2 nanosheets before and after the *operando* measurement without electrolyte, showing that both spectra are very similar and lack peaks around 214 cm^{-1}, 722 cm^{-1} and 812 cm^{-1}. This suggests that negligible photochemical damage occurred during the Raman measurements. We also confirmed that the *operando* Raman results are

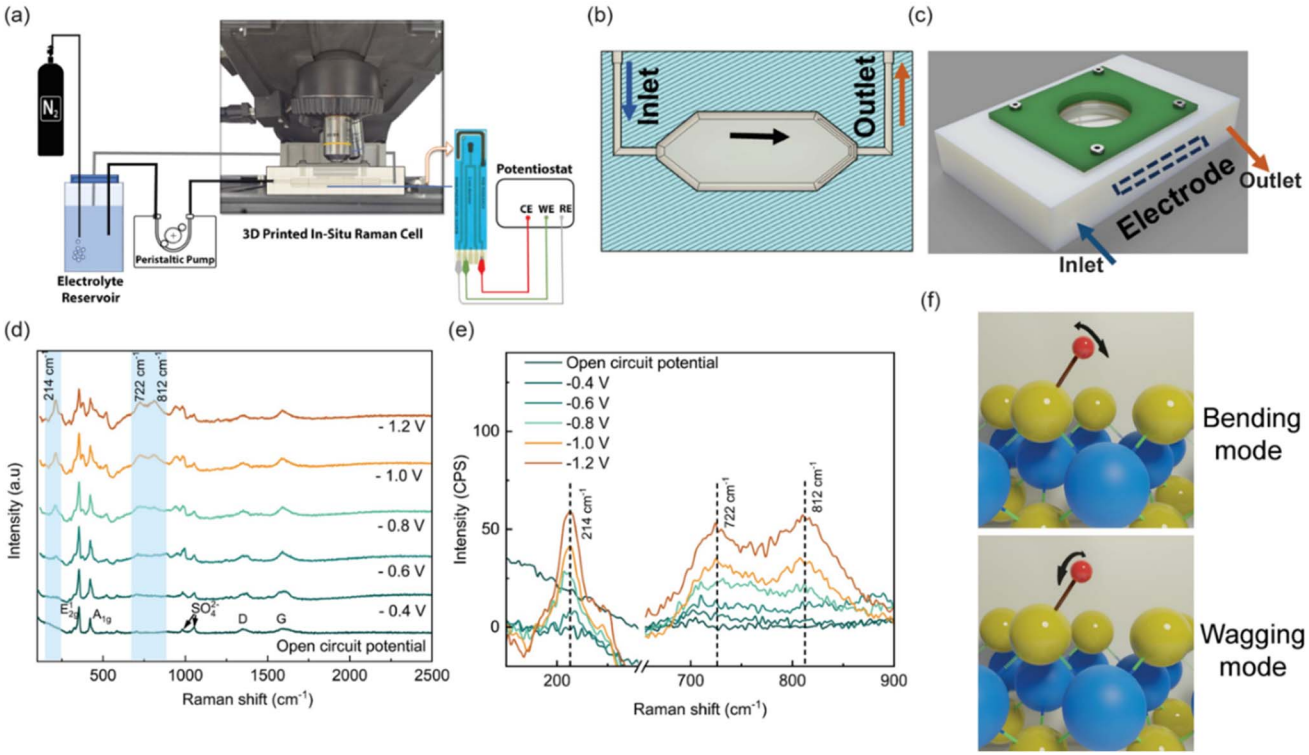

Fig. 5 (a–c) Schematic of experimental design and cell of *operando* Raman analysis (d) *operando* Raman spectra of the 50% WS_2 catalyst mixture in 0.5 M H_2SO_4 collected at different voltages (e) variation of Raman intensity of three peaks at 722 cm^{-1}, 812 cm^{-1} and 214 cm^{-1} with the increase of applied potential. (f) The bending (in-plane) and wagging (out of-plane) modes of H–S–W corresponding to the *operando* Raman signal and obtained through periodic DFT study.

reversible (Fig. S5e†) and reproducible in repeated trials (Fig. S5f†).

Periodic DFT calculations were carried out to augment the findings from *operando* Raman studies. H atom adsorption models on the WS_2 surface reveal a strong preference for the H atoms to occupy the S top site, as depicted in Fig. S6b and S6c.† The H–S bond distance is 1.43 Å with an angle of 53° with the nearest S atoms on the surface. Attempts to converge the H-atom adsorbed on to a W atom were unsuccessful, likely due to the stronger affinity of H–S bonding. The binding energy of an H atom on the surface of WS_2 was determined to be −0.50 eV. In contrast, the binding energy of an H atom with a subsurface S-atom was determined to be −0.19 eV (Fig. S6d and S6e†). Normal mode analyses resulted in no imaginary modes, confirming the ground state structures. The charge density difference plot (Fig. S7†) shows the interaction between the adsorbed H atom and the S atom. For H atoms adsorbed on surface S atoms (Fig. 5f), bending (in-plane vibrations) and wagging modes (out of-plane vibrations) were identified at 626 cm^{-1} and 554 cm^{-1}, respectively, closely matching the results of our *operando* Raman studies. All other modes corresponded to surface vibrations and frustrated translations.[60] The Raman vibration mode at 214 cm^{-1} could not be distinguished through the DFT calculations due to the occurrence of surface vibrations and frustrated translations in the low frequency range. The red shift of the DFT-derived vibrational modes with respect to experiment could result from the calculations not being performed in an aqueous medium and other complex experimental conditions that are not considered in this computational model.

Conclusion

This study presents a versatile, simple, and green synthesis of electrocatalytically active ultrathin WS_2 nanosheets for HER. The exfoliated WS_2 nanosheets produced by this approach are ultrathin (mono- to bi-layered) and single crystalline. XPS and HR-TEM analyses suggest that the nanosheets are predominantly in the semiconducting, hexagonal phase, with a minor fraction in the metallic phase. XPS and EDS analyses further confirm the high purity of the WS_2 nanosheets, while HR-STEM a high concentration of exposed active sites, including edge sites and structural defects.

Due to their high crystallinity, large surface area, abundant edge sites/defects, and clean surfaces, the WS_2 nanosheets exhibit outstanding HER performance. Notably, potential cycling activates the surface and enhances HER activity. *Operando* Raman spectroscopy provides valuable insights into the catalytic active sites of WS_2 nanosheets by monitoring the S–H reaction intermediate. Periodic DFT calculations further corroborate the bending and wagging vibrational modes of the S–H intermediate observed in *operando* Raman measurements.

In summary, this green and versatile synthesis method for highly exfoliated TMD nanosheets establishes a strong

foundation for efficient and sustainable hydrogen production. Future developments, such as doping and heterostructure formation, could further enhance their catalytic performance.

Data availability

The data underlying this study are available in the published article and its ESI.†

Author contributions

NLK, FY, and DYK participated in conceiving and designing the project. NLK and IYK conducted the exfoliation and synthesis of catalyst materials. NLK, NC, and USK contributed to electrochemical characterization and *in situ* Raman analysis. MG and BSG carried out high resolution STEM characterization. KRR and CR contributed to DFT calculations, while SS and AS performed AFM characterization.

Conflicts of interest

There are no conflicts to declare.

Acknowledgements

This work was supported by the National Science Foundation under OIA 2327349 (DYK, NC) and CBET 2018411 (FY, NLK), and partially by the donors of ACS Petroleum research Fund under New Directions Grant 67748-ND10 (DYK, NC). Partial salary support was provided by Southern company (NLK), the University of Kentucky College of Arts and Sciences (NLK, NC), and the U.S. Department of Energy under DE-SC0022315 (MDAG, BSG). BSG thanks the University of Kentucky's Frank J. Derbyshire Professorship. KRR and CR acknowledge funding by the Research Corporation for Science Advancement (RCSA) Cottrell Scholars program (Award No. 24432). SS and AS acknowledge the support of the National Science Foundation (grant no. DMR-2104296). High-resolution STEM imaging was conducted by Dr Matthew Boebinger at the Center for Nanophase Materials Sciences (CNMS), Oak Ridge National Laboratory which is a DOE Office of Science user facility. TEM and EDS characterization was performed at the Electron Microscopy Center (EMC), University of Kentucky, which belongs to the National Science Foundation NNCI Kentucky Multiscale Manufacturing and Nano Integration Node. Computing resources on the Lipscomb High Performance Computing Cluster were provided by the University of Kentucky Information Technology Department and the Center for Computational Sciences (CCS).

References

1 G. Eda, H. Yamaguchi, D. Voiry, T. Fujita, M. Chen and M. Chhowalla, Photoluminescence from Chemically Exfoliated MoS2, *Nano Lett.*, 2011, **11**(12), 5111–5116, DOI: **10.1021/nl201874w**.

2 Á. Coogan and Y. K. Gun'Ko, Solution-based "bottom-up" synthesis of group VI transition metal dichalcogenides and their applications, *Mater. Adv.*, 2021, **2**(1), 146–164, DOI: **10.1039/d0ma00697a**.

3 S. A. Han, R. Bhatia and S.-W. Kim, Synthesis, properties and potential applications of two-dimensional transition metal dichalcogenides, *Nano Converg.*, 2015, **2**, 1–14, DOI: **10.1186/s40580-015-0048-4**.

4 H. Jin, T. Song, U. Paik and S.-Z. Qiao, Metastable Two-Dimensional Materials for Electrocatalytic Energy Conversions, *Acc. Mater. Res.*, 2021, **2**, 559–573, DOI: **10.1021/accountsmr.1c00115**.

5 I. H. Kwak, I. S. Kwon, J. H. Lee, Y. R. Lim and J. Park, Chalcogen-vacancy group VI transition metal dichalcogenide nanosheets for electrochemical and photoelectrochemical hydrogen evolution, *J. Mater. Chem. C*, 2021, **9**(1), 101–109, DOI: **10.1039/d0tc04715e**.

6 M. Chhowalla, H. S. Shin, G. Eda, L.-J. Li, K. P. Loh and H. Zhang, The chemistry of two-dimensional layered transition metal dichalcogenide nanosheets, *Nat. Chem.*, 2013, **5**(4), 263–275, DOI: **10.1038/nchem.1589**.

7 D. Voiry, A. Mohite and M. Chhowalla, Phase engineering of transition metal dichalcogenides, *Chem. Soc. Rev.*, 2015, **44**(9), 2702–2712, DOI: **10.1039/c5cs00151j**.

8 M.-Y. Li, C.-H. Chen, Y. Shi and L.-J. Li, Heterostructures based on two-dimensional layered materials and their potential applications, *Mater. Today*, 2016, **19**(6), 322–335, DOI: **10.1016/j.mattod.2015.11.003**.

9 T. A. Shifa, F. Wang, Y. Liu and J. He, Heterostructures Based on 2D Materials: A Versatile Platform for Efficient Catalysis, *Adv. Mater.*, 2019, **31**(45), 1804828, DOI: **10.1002/adma.201804828**.

10 Y. Shi, Z. R. Ma, Y. Y. Xiao, Y. C. Yin, W. M. Huang, Z. C. Huang, Y. Z. Zheng, F. Y. Mu, R. Huang, G. Y. Shi, *et al.*, Electronic metal-support interaction modulates single-atom platinum catalysis for hydrogen evolution reaction, *Nat. Commun.*, 2021, **12**(1), 3021, DOI: **10.1038/s41467-021-23306-6**From NLM PubMed-not-MEDLINE.

11 D. Voiry, M. Salehi, R. Silva, T. Fujita, M. Chen, T. Asefa, V. B. Shenoy, G. Eda and M. Chhowalla, Conducting MoS2 Nanosheets as Catalysts for Hydrogen Evolution Reaction, *Nano Lett.*, 2013, **13**(12), 6222–6227, DOI: **10.1021/nl403661s**.

12 D. Y. Chung, S.-K. Park, Y.-H. Chung, S.-H. Yu, D.-H. Lim, N. Jung, H. C. Ham, H.-Y. Park, Y. Piao, S. J. Yoo, *et al.*, Edge-exposed MoS2nano-assembled structures as efficient electrocatalysts for hydrogen evolution reaction, *Nanoscale*, 2014, **6**(4), 2131–2136, DOI: **10.1039/c3nr05228a**.

13 J. Kibsgaard, Z. Chen, B. N. Reinecke and T. F. Jaramillo, Engineering the surface structure of MoS2 to preferentially expose active edge sites for electrocatalysis, *Nat. Mater.*, 2012, **11**(11), 963–969, DOI: **10.1038/nmat3439**.

14 D. Voiry, H. Yamaguchi, J. Li, R. Silva, D. C. B. Alves, T. Fujita, M. Chen, T. Asefa, V. B. Shenoy, G. Eda, *et al.*, Enhanced catalytic activity in strained chemically exfoliated WS2 nanosheets for hydrogen evolution, *Nat. Mater.*, 2013, **12**(9), 850–855, DOI: **10.1038/nmat3700**.

15 L. Wang, G. Zhou, H. Luo, Q. Zhang, J. Wang, C. Zhao, A. M. Rao, B. Xu and B. Lu, Enhancing catalytic activity of tungsten disulfide through topology, *Appl. Catal. B Environ.*, 2019, **256**, 117802, DOI: 10.1016/j.apcatb.2019.117802.

16 S. Xu, D. Li and P. Wu, One-Pot, Facile, and Versatile Synthesis of Monolayer MoS_2/WS_2Quantum Dots as Bioimaging Probes and Efficient Electrocatalysts for Hydrogen Evolution Reaction, *Adv. Funct. Mater.*, 2015, **25**(7), 1127–1136, DOI: 10.1002/adfm.201403863.

17 P. May, U. Khan, J. M. Hughes and J. N. Coleman, Role of Solubility Parameters in Understanding the Steric Stabilization of Exfoliated Two-Dimensional Nanosheets by Adsorbed Polymers, *J. Phys. Chem. C*, 2012, **116**(20), 11393–11400, DOI: 10.1021/jp302365w.

18 L. Niu, J. N. Coleman, H. Zhang, H. Shin, M. Chhowalla and Z. Zheng, Production of Two-Dimensional Nanomaterials via Liquid-Based Direct Exfoliation, *Small*, 2016, **12**(3), 272–293, DOI: 10.1002/smll.201502207.

19 J. N. Coleman, Liquid Exfoliation of Defect-Free Graphene, *Acc. Chem. Res.*, 2013, **46**(1), 14–22, DOI: 10.1021/ar300009f.

20 J. M. Hughes, D. Aherne and J. N. Coleman, Generalizing solubility parameter theory to apply to one- and two-dimensional solutes and to incorporate dipolar interactions, *J. Appl. Polym. Sci.*, 2013, **127**(6), 4483–4491, DOI: 10.1002/app.38051.

21 V. Nicolosi, M. Chhowalla, M. G. Kanatzidis, M. S. Strano and J. N. Coleman, Liquid Exfoliation of Layered Materials, *Science*, 2013, **340**(6139), 1226419, DOI: 10.1126/science.1226419.

22 A. Sajedi-Moghaddam and E. Saievar-Iranizad, High-yield exfoliation of tungsten disulphide nanosheets by rational mixing of low-boiling-point solvents, *Mater. Res. Express*, 2018, **5**(1), DOI: 10.1088/2053-1591/aaa500.

23 C.-J. Shih, S. Lin, M. S. Strano and D. Blankschtein, Understanding the Stabilization of Liquid-Phase-Exfoliated Graphene in Polar Solvents: Molecular Dynamics Simulations and Kinetic Theory of Colloid Aggregation, *J. Am. Chem. Soc.*, 2010, **132**(41), 14638–14648, DOI: 10.1021/ja1064284.

24 H. C. Yau, M. K. Bayazit, J. H. Steinke and M. S. Shaffer, Sonochemical degradation of N-methylpyrrolidone and its influence on single walled carbon nanotube dispersion, *Chem. Commun.*, 2015, **51**(93), 16621–16624, DOI: 10.1039/c5cc06526g.

25 R. Jha and P. K. Guha, An effective liquid-phase exfoliation approach to fabricate tungsten disulfide into ultrathin two-dimensional semiconducting nanosheets, *J. Mater. Sci.*, 2017, **52**(12), 7256–7268, DOI: 10.1007/s10853-017-0962-4.

26 G. Kresse and J. Furthmüller, Efficiency of ab-initio total energy calculations for metals and semiconductors using a plane-wave basis set, *Comput. Mater. Sci.*, 1996, **6**(1), 15–50, DOI: 10.1016/0927-0256(96)00008-0.

27 G. Kresse and J. Furthmüller, Efficient iterative schemes for *ab initio* total-energy calculations using a plane-wave basis set, *Phys. Rev. B:Condens. Matter Mater. Phys.*, 1996, **54**(16), 11169–11186, DOI: 10.1103/physrevb.54.11169.

28 G. Kresse and J. Hafner, *Ab initio* molecular dynamics for liquid metals, *Phys. Rev. B:Condens. Matter Mater. Phys.*, 1993, **47**(1), 558–561, DOI: 10.1103/physrevb.47.558.

29 G. Kresse and D. Joubert, From ultrasoft pseudopotentials to the projector augmented-wave method, *Phys. Rev. B:Condens. Matter Mater. Phys.*, 1999, **59**(3), 1758–1775, DOI: 10.1103/physrevb.59.1758.

30 J. P. Perdew, K. Burke and M. Ernzerhof, Generalized Gradient Approximation Made Simple, *Phys. Rev. Lett.*, 1996, **77**(18), 3865–3868, DOI: 10.1103/physrevlett.77.3865.

31 W. H. Press, S. A. Teukolsky, W. T. Vetterling and B. P. Flannery, *NUMERICAL RECIPES the Art of Scientific Computing*, Cambridge University Press, 3rd edn, 1986, pp. 515–520.

32 A. Jain, S. P. Ong, G. Hautier, W. Chen, W. D. Richards, S. Dacek, S. Cholia, D. Gunter, D. Skinner, G. Ceder, *et al.*, Commentary: The Materials Project: a materials genome approach to accelerating materials innovation, *APL Mater.*, 2013, **1**, 1–11, DOI: 10.1063/1.4812323.

33 G. Henkelman, G. Jóhannesson and H. Jónsson, Methods for Finding Saddle Points and Minimum Energy Paths, in *Theoretical Methods in Condensed Phase Chemistry*, ed. S. D. Schwartz, Springer Netherlands, 2002, pp. 269–302.

34 G. Vazquez, E. Alvarez and J. M. Navaza, Surface tension of alcohol water+ water from 20 to 50. degree. C, *J. Chem. Eng. Data*, 1995, **40**(3), 611–614.

35 S. Lin, C.-J. Shih, M. S. Strano and D. Blankschtein, Molecular Insights into the Surface Morphology, Layering Structure, and Aggregation Kinetics of Surfactant-Stabilized Graphene Dispersions, *J. Am. Chem. Soc.*, 2011, **133**(32), 12810–12823, DOI: 10.1021/ja2048013.

36 A. Berkdemir, H. R. Gutiérrez, A. R. Botello-Méndez, N. Perea-López, A. L. Elías, C.-I. Chia, B. Wang, V. H. Crespi, F. López-Urías, J.-C. Charlier, *et al.*, Identification of individual and few layers of WS2 using Raman Spectroscopy, *Sci. Rep.*, 2013, **3**, 1755, DOI: 10.1038/srep01755.

37 T. A. J. Loh, D. H. C. Chua and A. T. S. Wee, One-step Synthesis of Few-layer WS2 by Pulsed Laser Deposition, *Sci. Rep.*, 2016, **5**, 18116, DOI: 10.1038/srep18116.

38 P. Saha, B. Ghosh, R. Jana and G. Dev Mukherjee, Structural anomalies in exfoliated WS2: high pressure investigations on monolayer and nanocrystalline tungsten disulfide, *J. Appl. Phys.*, 2018, **123**, 204306, DOI: 10.1063/1.5027020.

39 Z. Liu, N. Li, C. Su, H. Zhao, L. Xu, Z. Yin, J. Li and Y. Du, Colloidal synthesis of 1T' phase dominated WS2 towards endurable electrocatalysis, *Nano Energy*, 2018, **50**, 176–181, DOI: 10.1016/j.nanoen.2018.05.019.

40 B. J. Carey, T. Daeneke, E. P. Nguyen, Y. Wang, J. Zhen Ou, S. Zhuiykov and K. Kalantar-Zadeh, Two solvent grinding sonication method for the synthesis of two-dimensional tungsten disulphide flakes, *Chem. Commun.*, 2015, **51**(18), 3770–3773, DOI: 10.1039/c4cc08399g.

41 W. Liu, J. Benson, C. Dawson, A. Strudwick, A. P. A. Raju, Y. Han, M. Li and P. Papakonstantinou, The effects of exfoliation, organic solvents and anodic activation on the catalytic hydrogen evolution reaction of tungsten disulfide,

Nanoscale, 2017, **9**(36), 13515–13526, DOI: 10.1039/c7nr04790h.

42 T. P. Nguyen, S. Choi, J.-M. Jeon, K. C. Kwon, H. W. Jang and S. Y. Kim, Transition Metal Disulfide Nanosheets Synthesized by Facile Sonication Method for the Hydrogen Evolution Reaction, *J. Phys. Chem. C*, 2016, **120**(7), 3929–3935, DOI: 10.1021/acs.jpcc.5b12164.

43 B. Mahler, V. Hoepfner, K. Liao and G. A. Ozin, Colloidal synthesis of 1T-WS2 and 2H-WS2 nanosheets: applications for photocatalytic hydrogen evolution, *J. Am. Chem. Soc.*, 2014, **136**(40), 14121–14127, DOI: 10.1021/ja506261tFrom NLM PubMed-not-MEDLINE.

44 Q. H. Wang, K. Kalantar-Zadeh, A. Kis, J. N. Coleman and M. S. Strano, Electronics and optoelectronics of two-dimensional transition metal dichalcogenides, *Nat. Nanotechnol.*, 2012, **7**(11), 699–712, DOI: 10.1038/nnano.2012.193.

45 M. P. Thomas, N. Wanninayake, M. De Alwis Goonatilleke, D. Y. Kim and B. S. Guiton, Direct imaging of heteroatom dopants in catalytic carbon nano-onions, *Nanoscale*, 2020, **12**(10), 6144–6152, DOI: 10.1039/d0nr00335b.

46 X. Sang, X. Li, W. Zhao, J. Dong, C. M. Rouleau, D. B. Geohegan, F. Ding, K. Xiao and R. R. Unocic, In situ edge engineering in two-dimensional transition metal dichalcogenides, *Nat. Commun.*, 2018, **9**, 2051, DOI: 10.1038/s41467-018-04435-x.

47 G. Eda, T. Fujita, H. Yamaguchi, D. Voiry, M. Chen and M. Chhowalla, Coherent Atomic and Electronic Heterostructures of Single-Layer MoS_2, *ACS Nano*, 2012, **6**(8), 7311–7317, DOI: 10.1021/nn302422x.

48 S. Wang, G.-D. Lee, S. Lee, E. Yoon and J. H. Warner, Detailed Atomic Reconstruction of Extended Line Defects in Monolayer MoS_2, *ACS Nano*, 2016, **10**(5), 5419–5430, DOI: 10.1021/acsnano.6b01673.

49 R. G. Mendes, J. Pang, A. Bachmatiuk, H. Q. Ta, L. Zhao, T. Gemming, L. Fu, Z. Liu and M. H. Rümmeli, Electron-Driven *In Situ* Transmission Electron Microscopy of 2D Transition Metal Dichalcogenides and Their 2D Heterostructures, *ACS Nano*, 2019, **13**, 978–995, DOI: 10.1021/acsnano.8b08079.

50 L. Wu, A. J. Van Hoof, N. Y. Dzade, L. Gao, M.-I. Richard, H. Friedrich, N. H. De Leeuw, E. J. Hensen and J. P. Hofmann, Enhancing the electrocatalytic activity of 2H-WS 2 for hydrogen evolution via defect engineering, *Phys. Chem. Chem. Phys.*, 2019, **21**(11), 6071–6079.

51 L. Liao, Y. Zhao, H. Zhou, D. Li, Y. Qi, Y. Zhang, Y. Sun, Q. Zhou and F. Yu, Edge-oriented N-Doped WS(2) Nanoparticles on Porous Co(3) N Nanosheets for Efficient Alkaline Hydrogen Evolution and Nitrogenous Nucleophile Electrooxidation, *Small*, 2022, **18**(40), e2203171, DOI: 10.1002/smll.202203171From NLM PubMed-not-MEDLINE.

52 H. Chen, Y. Li, H. Huang, Q. Kang and T. Ma, Petal-like FexSy/WS2 Heterojunction Nanosheets as an Electrocatalyst for Highly Effective Hydrogen Evolution Reaction, *Energy Fuels*, 2022, **36**(9), 4888–4894, DOI: 10.1021/acs.energyfuels.2c00483.

53 S. Saifi, G. Dey, J. Karthikeyan, A. S. K. Sinha and A. Aijaz, MoS2 and WS2 Nanosheets Decorated on Metal–Organic Framework-Derived Cobalt/Carbon Nanostructures as Electrocatalysts for Hydrogen Evolution, *ACS Appl. Nano Mater.*, 2022, **5**(8), 10696–10703, DOI: 10.1021/acsanm.2c02028.

54 L. Sun, M. Gao, Z. Jing, Z. Cheng, D. Zheng, H. Xu, Q. Zhou and J. Lin, 1 T-Phase Enriched P doped WS2 nanosphere for highly efficient electrochemical hydrogen evolution reaction, *Chem. Eng. J.*, 2022, **429**, 132187.

55 T. Shinagawa, A. T. Garcia-Esparza and K. Takanabe, Insight on Tafel slopes from a microkinetic analysis of aqueous electrocatalysis for energy conversion, *Sci. Rep.*, 2015, **5**(1), 13801.

56 J. Shi, X. Wang, S. Zhang, L. Xiao, Y. Huan, Y. Gong, Z. Zhang, Y. Li, X. Zhou, M. Hong, *et al.*, Two-dimensional metallic tantalum disulfide as a hydrogen evolution catalyst, *Nat. Commun.*, 2017, **8**, 958, DOI: 10.1038/s41467-017-01089-z.

57 P. Afanasiev and H. Jobic, On hydrogen adsorption by nanodispersed MoS2-based catalysts, *J. Catal.*, 2021, **403**, 111–120, DOI: 10.1016/j.jcat.2020.12.020.

58 C. J. Wright, D. Fraser, R. B. Moyes and P. B. Wells, The adsorption of hydrogen and hydrogen sulphide on tungsten sulphide; isotherm and neutron scattering studies, *Appl. Catal.*, 1981, **1**(1–2), 49–58, DOI: 10.1016/0166-9834(81)80017-6.

59 M. Hartnett and S. Fahy, Vibrational mode frequencies of H2S and H2O adsorbed on Ge(001)-(2×1) surfaces, *Appl. Surf. Sci.*, 2015, **329**, 363–370, DOI: 10.1016/j.apsusc.2014.12.096.

60 A. A. Gokhale, S. Kandoi, J. P. Greeley, M. Mavrikakis and J. A. Dumesic, Molecular-level descriptions of surface chemistry in kinetic models using density functional theory, *Chem. Eng. Sci.*, 2004, **59**(22), 4679–4691, DOI: 10.1016/j.ces.2004.09.038.